# Hydrothermal synthesis of mixed crystal phases TiO₂–reduced graphene oxide nanocomposites with small particle size for lithium ion batteries

*Lei Dong [a,1], Minsi Li [b,1], Lei Dong [a,1], Mengli Zhao [a], Jianmin Feng [a], Yan Han [a], Jianhua Deng [a], Xifei Li [a], Dejun Li [a,\*], Xueliang Sun [c,\*\*]*

[a] College of Physics and Materials Science, Tianjin Normal University, Tianjin 300387, China
[b] School of Chemistry and Materials Science, University of Science and Technology of China, Hefei, Anhui 230026, China
[c] Department of Mechanical and Materials Engineering, Western University, London, Ontario, Canada

## ARTICLE INFO

## ABSTRACT

A rutile and anatase mixed crystal phase of nano-rod TiO₂ and TiO₂–reduced graphene oxide (TiO₂–RGO) nanocomposites with small particle size were prepared via a facile hydrothermal approach with titanium tetrabutoxide and graphene oxide as the precursor. Hydrolysis of titanium tetrabutoxide and mild reduction of graphene oxide were simultaneously carried out. Compared with traditional multistep methods, a novel green synthetic route to produce TiO₂–RGO without toxic solvents or reducing agents was employed. TiO₂–RGO as anode of lithium ion batteries was characterized by extensive measurements. The nanocomposites exhibited notable improvement in lithium ion insertion/extraction behavior compared with TiO₂, indicating an initial irreversible capacity and a reversible capacity of 295.4 and 112.3 mA h g$^{-1}$ for TiO₂–RGO after 100 cycles at a high charge rate of 10 C. The enhanced electrochemical performance is attributed to increased conductivity in presence of reduced graphene oxide in TiO₂–RGO, a rutile and anatase mixed crystal phase of nano-rod TiO₂/GNS composites, small size of TiO₂ particles in nanocomposites, and enlarged electrode–electrolyte contact area, leading to more electroactive sites in TiO₂–RGO.

## 1. Introduction

Electrochemical energy storage has attracted great attention after the oil crisis. Currently, as energy storage devices dominating power sources, Lithium ion batteries are being considered as the candidates for hybrid vehicles [1], and all electrical vehicles, and possibly for utility applications as well, have attracted considerable attention in the scientific and industrial communities [2]. Although the lithium ion battery is a promising device for energy storage, its electromotive force, energy density, needs to be improved [3].

---

\* *Corresponding author.* Tel./fax: +86 22 23766519.
\*\* *Corresponding author.* Tel.: +1 519 661 2111x87759; fax: +1 519 661 3020.
  E-mail addresses: dejunli@mail.tjnu.edu.cn, dli1961@126.com (D. Li), xsun@eng.uwo.ca (X. Sun).
  [1] Lei Dong, Minsi Li, Lei Dong contributed equally to this work.

$TiO_2$ is a fast and low voltage insertion host for Li and an abundant, low cost, and environmentally benign electrode material [4]. Besides, during Li insertion/extraction, $TiO_2$ can remain structurally stable, and it is free of electrochemical Li deposition, which is important for the safe operation of LIBs. $TiO_2$ has attracted tremendous research interests as anode materials for lithium ion batteries [5,6]. However, the cycling performance of $TiO_2$ electrodes at high discharge/charge rates is still poor owing to the poor electron transport in $TiO_2$, and relatively, the low theoretic capacity is still the main problem for their practical applications. In addition, $TiO_2$ agglomeration and dissolution during the high discharge/charge cycling processes will lead to reduction of reversible performance. Nanostructured $TiO_2$ has been studied for Li-insertion because it is a low-voltage insertion host for $Li^+$, and also a fast Li insertion/extraction host [7]. Nano-scale active materials can get higher capacities and higher rate capabilities than their bulk counterparts in the electrodes of lithium rechargeable batteries due to their higher surface area [8,9]. Various $TiO_2$ nanostructures, showing improved performances, have been achieved, such as nanotubes, nanowires and nanorods [10]. As a result, in order to get useable $TiO_2$ nanoparticles, development of exact synthetic techniques is important [10]. In addition, the morphology of two dimensional graphene or reduced graphene oxide (RGO) sheets is favorable for retaining the stable structures of the anode materials in the charging and discharging processes [11]. Graphene and RGO nanosheets are promising substrate for nanocomposites materials of LIBs [12]. Hence, the $TiO_2$ agglomeration and dissolution problem could be surmounted by employing $TiO_2$–RGO hybrid nanocomposites instead of $TiO_2$ nanoparticles. However, the layered RGO sheets can unaffectedly stack into multilayers and lose the advantages of high surface area and high electron mobility. $TiO_2$ anchored on the RGO sheets could potentially resolve the problem of RGO stacking [13–15].

In this work, graphene oxide (GO) was successfully synthesized using graphite as the starting material, then the rutile and anatase mixed crystal phase of nano-rod $TiO_2$–RGO composites were obtained from tetrabutyl titanate and GO aqueous solution by a one-step hydrothermal method (Scheme 1). The as-prepared nanocomposites were used as anode for LIBs. The performance of the resultant LIBs was evaluated systematically.

## 2. Experimental

### 2.1. Preparation of materials

#### 2.1.1. Synthesis of graphene oxide
GO was synthesized via the oxidation of graphite using the improved Hummers' method, the oxidation method proposed by Tour's group [16]. Briefly, at the beginning, a 9:1 mixture of concentrated $H_2SO_4/H_3PO_4$ (180:20 ml) was added to a mixture of graphite flakes (3.0 g, 1 wt equiv) and $KMnO_4$ (12.0 g, 4 wt equiv) at room temperature. The reactants were heated to 50 °C and stirred for 24 h. Next, the products were cooled to 20 °C and poured onto ice (300 ml) with 30% $H_2O_2$ (20 ml). Then, the mixture color turned into golden yellow from turquoise and was centrifuged (12,000 rpm for 20 min). The supernatant was decanted away and the remaining solid was washed in succession with 5% HCL until the $SO_4^{2+}$ could not be checked out by the $BaSO_4$. Finally, the suspension material was washed in succession with deionized water until the pH value of the filtrate was nearly neutral. Suspension material was dried overnight at room temperature to get graphene oxide.

#### 2.1.2. Synthesis of $TiO_2$–reduced graphene oxide nanocomposites
First, titanium tetrabutoxide (3 ml) was drop wise added into the mixture of ethanol (2.5 ml) and hydrochloric acid (3.5 ml) to obtain a clear solution under magnetic stirring. Then, the above solution was added to the aqueous suspension of GO to meet a total volume of 40 ml. After stirred for another 0.5 h, the whole mixture was transferred into a 50 ml Teflon-lined stainless steel autoclave and sealed, heated to 160 °C and then kept for 12 h. After cooling to room temperature naturally, the resulting solid was washed with water and dried at 140 °C under vacuum. Then it was heated to 350 °C with a heating rate of 10 °C min$^{-1}$ in Ar flow, and $TiO_2$–RGO composite as a blue–black powder was obtained. At the same time, the above solution was diluted by distilled water to meet a total volume of 40 ml. The obtained white powder was centrifuged, rinsed with distilled water repeatedly, and finally dried at 333 K under vacuum, $TiO_2$ as a milky white color powder was successfully prepared [13].

### 2.2. Structure and morphology characterization

XRD (Rigaku D/MAX 2500 X), FTIR (IRAffinity-1), and SEM (Nova Nano SEM 230) were used to analyze the structure and morphologies of graphene. The Raman spectrum was measured by a laser Raman Spectrometer (Renishaw-1000) at an output power of 1.55 mW of 785 nm He–Ne laser.

### 2.3. Electrochemical measurements

The electrochemical performances of the samples were measured as follow. Sample powders were mixed in N-methylpyrrolidone (NMP) with 10 wt% acetylene black and 10 wt% polyvinylidene fluoride (PVDF) binder. The electrolyte composed of 1 M $LiPF_6$ dissolved in ethylene carbonate (EC) and diethyl carbonate (DEC) with a volume ratio of 1:1. After drying 24 h under vacuum at 100 °C, the anode was assembled
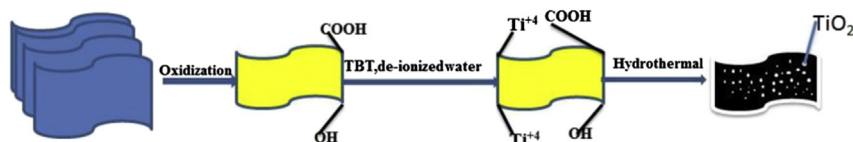


Scheme 1 – Illustration of the synthesis process of $TiO_2$–RGO from GO.

into CR-2032-type coin half-cells using lithium foil as the counter electrode in glove box (M/Braun, moisture and oxygen concentration <1 ppm). The charge/discharge experiments were performed on Land CT 2001A (China) in the voltage range of 3.0–1.0 V vs. Li$^+$/Li at different rates. Electrochemical impedance spectroscopy (EIS) measurements of the electrodes were also performed on the electrochemical workstation Versa STAT 4 (Princeton Applied Research) using the frequency response analysis applying a sine wave with amplitude of 5.0 mV over the frequency range from 100 kHz to 0.001 Hz.

## 3. Results and discussion

The structural compositions of GO, RGO, TiO$_2$, and TiO$_2$–RGO nanocomposites examined by XRD are shown in Fig. 1. The pattern of GO shows a major peak at $2\theta = 10.4°$, corresponding to a d-spacing of 0.95 nm, which is much larger than the d-spacing of natural graphite at 0.335 nm. This change indicates that graphite was oxidized to GO [17]. As shown in the diffractogram, pure TiO$_2$ synthesized by the hydrothermal route showed perfect crystallinity. The peaks of $2\theta$ values at 25.3°, 37.9°, 48.0°, 54.4°, 56.6°, 62.8°, and 68.9° can be indexed to (101), (004), (200), (105), (211), (204), and (116) planes of anatase titania, respectively. On the other hand, the characteristic diffraction peaks at $2\theta$ values 27.4°, 27.8°, 36.1°, and 41.3° are assigned to (110), (101), and (111) crystal faces of rutile TiO$_2$. The peaks corresponding to the anatase and rutile phases are denoted by "a" and "r", respectively. The diffraction peak for RGO was appearing at a $2\theta$ angle of 24.57°. The TiO$_2$–RGO composites exhibits similar diffraction peaks corresponding to pure TiO$_2$ particles, meaning a rutile and anatase mixed crystal phase of nano-rod TiO$_2$/GNS composites has been prepared by hydrothermal process. Nonetheless, the peaks corresponding to RGO in the TiO$_2$–RGO composite cannot be observed. This phenomenon is ascribed to the in short supply of carbon and relatively low diffraction intensity of the RGO in the research [18]. In this work, no peaks for graphite ($2\theta = 26.6°$) can be observed, suggesting no further agglomeration of few-layer RGO sheets which were hindered by TiO$_2$
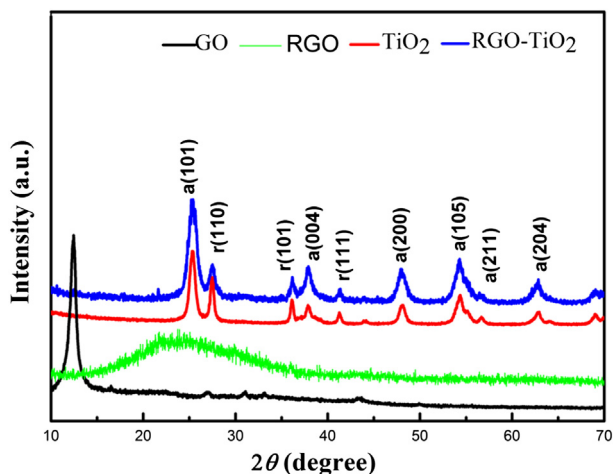
nanoparticles [19]. This result implies the RGO sheets were scattered into the TiO$_2$ nanoparticles. This will be further demonstrated by Raman data.

Fig. 2a shows the representative thermogravimetric analysis (TGA) curve of the GO and TiO$_2$–RGO nanocomposites. According to the mass loss of graphene in nanocomposites, about 94.4 wt% of TiO$_2$ was deposited on the surface of RGO nanosheets matrix. In order to confirm the chemical composition of the composite, Raman spectroscopy was used to characterize the TiO$_2$–RGO nanocomposites as well as the as-prepared GO in Fig. 2b. Typical peaks ascribed to anatase TiO$_2$ Raman peak is clearly seen at about 143 cm$^{-1}$, which is attributed to the main anatase vibration mode. Furthermore, vibration peaks at 444 cm$^{-1}$, 604 cm$^{-1}$ are also characteristic of rutile TiO$_2$ compared with that of GO in Fig. 2b in the range of 100–800 cm$^{-1}$ [20,21]. Fig. 2b shows that the rutile and anatase mixed crystal phase of TiO$_2$ coexist. This is consistent with the reported XRD pattern in Fig. 1. According to the results examined by the TGA, the as-prepared composite contains 5.6% (w/w) of RGO. In Raman spectra, both samples exhibit two strong peaks, denoted as the disorder peak (D, centered at ∼1316 cm$^{-1}$) and the graphitic peak (G, at ∼1595 cm$^{-1}$). Compared to the spectrum of GO, the D band and G band of TiO$_2$–RGO are blue shifted slightly and their intensities decreased, implies the change of functional groups on the carbon network of GO by hydrothermal conversion [22]. The intensity ratio of the D and G bands (ID/IG) decreases a little after hydrothermal treatment (1.15 vs. 1.26), this result seems
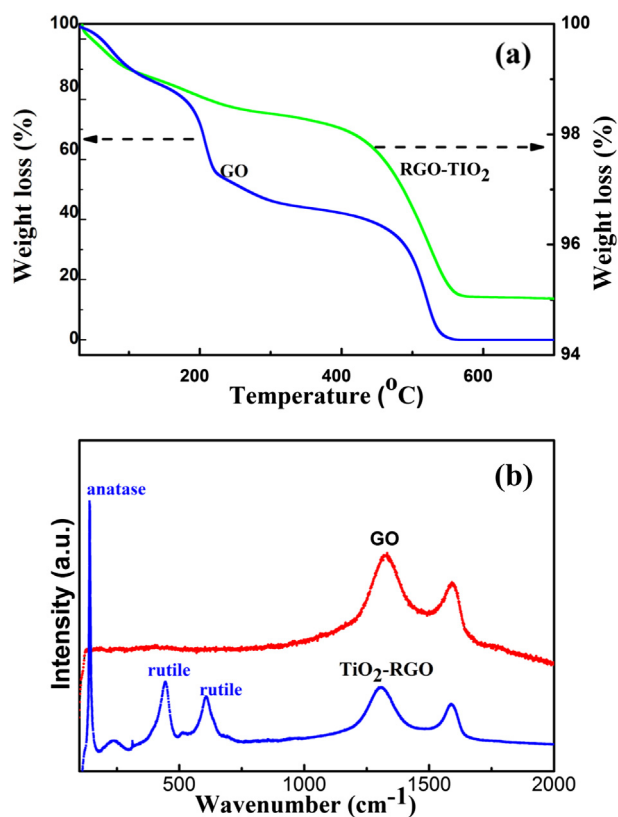




Fig. 2 – (a) Thermogravimetric analysis (TGA) curve of GO, TiO$_2$–RGO composite and (b) Raman spectra of the TiO$_2$–RGO composite.



Fig. 1 – XRD patterns of, GO, RGO, TiO2 and TiO$_2$–RGO.

to indicate that graphitic (sp$^2$) nature of the carbon in the hydrothermal treatment remained the same after loading with $TiO_2$ [23].

Fig. 3 shows Fourier transform infrared spectroscopy (FTIR) spectra of the synthesized $TiO_2$, GO and $TiO_2$–RGO nanocomposites. The FTIR spectra of the synthesized $TiO_2$ shows a broad band below 1000 cm$^{-1}$, which is attributed to the Ti–O–Ti stretching and bending vibrational modes. It also shows a band at around 3400 cm$^{-1}$, which is due to the O–H stretching frequency from the surface hydroxyl group [24]. The peak at 1630 cm$^{-1}$ originates from the hydroxyl groups of molecular water. As a control, the GO spectrum is shown in Fig. 3. The spectrum of GO exhibits representative peaks at 3435, 1730, 1630, 1235 and 1061 cm$^{-1}$ corresponding to O–H stretch, C=O stretch, aromatic C=C and O–H bending, epoxy C–O stretch and alkoxy C–O stretch [25]. These evidences indicate that during the oxidation process of the graphite powder, the original extended conjugated π-orbital systems of the graphite are opened and oxygen-containing functional groups are inserted into carbon. The spectrum of RGO also shows absorption bands at 1630–1746 cm$^{-1}$, which are attributed to the stretching vibration of C–C and C–O groups of the residual COOH groups of RGO, respectively [26]. The peak at 2300 cm$^{-1}$ originates from the $CO_2$ In the air. This peak is also observed in the spectrum of $TiO_2$–RGO composite. All of the characteristic peaks of RGO are present in the $TiO_2$–RGO composite, as shown in the corresponding spectrum which means the reduction of GO to RGO is uncompleted by the thermal treatment process. And these results imply that GO was not reduced completely to graphene, and was instead mildly reduced to a RGO product, which contains remaining oxygen containing functional groups, such as –OH and –COOH [27]. Therefore, $TiO_2$ can be receptive to the interactions with these functional groups of RGO in the nanocomposites.

The SEM images show that the prepared $TiO_2$ has the morphology of nanorods. These nanorods were of 25–30 nm in diameter and 80–100 nm in length. Fig. 4 shows that the $TiO_2$ nanoparticles were well dispersed and uniformly anchored on the surface of the RGO sheet, small particle sizes $TiO_2$–RGO from 5 nm to 20 nm in diameter. The SEM image of the small particle sizes $TiO_2$–RGO demonstrates the
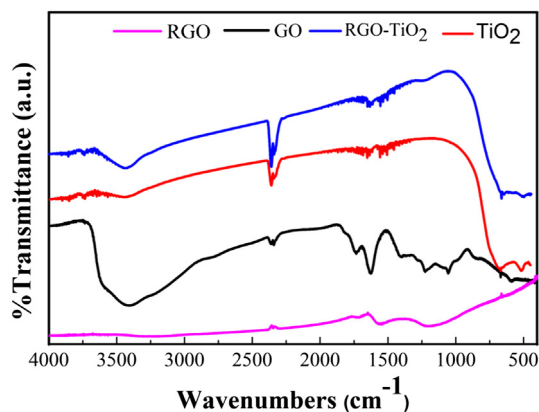
homogeneity of the composite in a large scale. In particular, only a small portion of RGO sheets and trace amount of free standing $TiO_2$ can be observed, while most of the RGO sheets were covered by the $TiO_2$ nanoparticles (i.e., RGO-bonded $TiO_2$). Also, majority of the $TiO_2$ particles were anchored on the RGO sheets (with very small amount of free standing $TiO_2$ nanoparticles), which is very important, because this ensures the efficient electron collection via the RGO sheets during the insertion/extraction processes [28] The SEM images reveal that the particles were in an aggregated state due to their extremely small dimensions and high surface energies.

Fig. 5 displays the voltage profiles of electrochemical cells made of the $TiO_2$–RGO nanocomposites at a rate of 10 C in the voltage range 1.0–3.0 V (vs. Li$^+$/Li). The C-rate is defined as the time in hours required to fully charge or discharge a battery [29]. Thus, n C-rate corresponds to the full discharge in 1/n hour [30]. It is well established that the lithium ion insertion/extraction processes at $TiO_2$ nanoparticles proceed according to a reversible reaction:

$$TiO_2 + xLi^+ + xe^- \leftrightarrow Li_xTiO_2$$
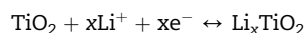
The maximum value of X for a reversible reaction at room temperature is 0.5 which corresponds to a capacity of 168 mA h/g [31]. Usually, the voltage window for $TiO_2$-based anode materials is 1–3 V, because RGO contributes charge and discharge capacity under 1 V. Besides, this can greatly minimize the formation of a solid electrolyte interface (SEI) layer. The SEI formation is usually one of the main reasons related to the irreversible capacity of the anode. If the cutoff voltage is greater than 1 V, SEI seldom occurs on $TiO_2$ electrodes [31]. Hence we set the voltage window between 1 V and 3 V [22]. Fig. 5 presents the charge/discharge profiles of the $TiO_2$–RGO composite electrode of the 1st, 2nd, 10th, and 100th cycles at a current density of 1000 mA/g. Significantly, the first discharge capacity is found up to 275.3 mA h/g, corresponding to a nominal insertion coefficient of x = 1.64. This value is larger than the theoretical capacity of $TiO_2$, suggesting the existence of additional lithium storage sites in the nanocomposites. A similar phenomenon has also been observed in $TiO_2$ hollow colloid anode materials [32]. This irreversible Li storage is attributed to the Li surface storage in the mixture RGO-based $TiO_2$ nanostructure [33]. Following Li-release processes up to 3.0 V yielded a Coulombic capacity of 164.89 mA h/g, accompanied by a 40.1% loss of the initial discharge. The initial reversible capacities at 2nd, 50th, and 100th cycles are 163.9, 138.4, and 113.3 mA h/g at a 10 C rate condition, respectively. The reversible capacity fade from the 2nd cycle to the 100th cycle is about ~0.51 mA h/g per cycle. The Coulombic efficiencies change from 59.8% at the 1st cycle to 92.2% at the 2nd cycle, 97.5% at the 50th cycle, and 99.1% at the 100th cycle. The low Coulombic efficiency is a common phenomenon for $TiO_2$-based materials, which is attributed to the Li surface storage in nanostructured $TiO_2$ to form conductive $Li_xTiO_2$ in the solid-solution domain [34]. Although the Coulombic efficiency of the first cycle is low, it is improved greatly upon cycling, which shows an increase to 99.1% at the 100th cycle. The discharge and charge plateaus of $TiO_2$–RGO for the first cycle are located at ~1.70 V (discharging process, Li insertion) and ~2.05 V (charging process, Li extraction), respectively. Over all, small

**Fig. 3 – FT-IR spectra of $TiO_2$, GO and $TiO_2$–RGO nanocomposites.**
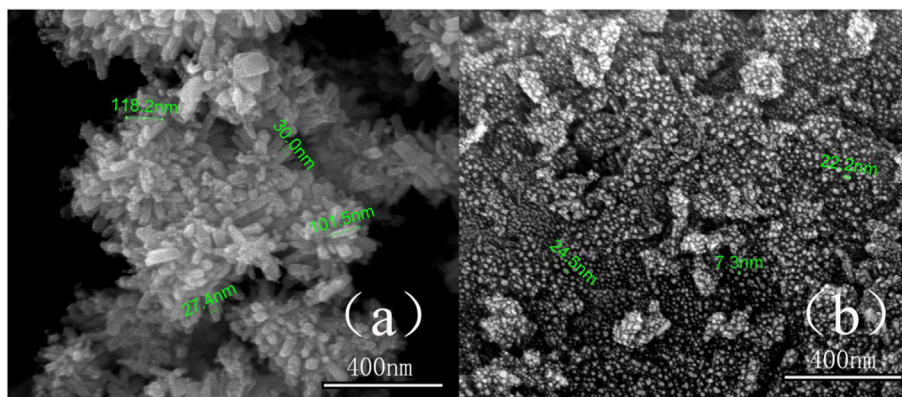
Fig. 4 — HRTEM images of the $TiO_2$ (a) and $TiO_2$—RGO (b) nanocomposites.

particle size $TiO_2$ particle and graphene sheets prevent the aggregation of the $TiO_2$ nanoparticles, increasing electrochemical reactive activity and thus increasing the specific charge capacity of the $TiO_2$ in $TiO_2$—RGO nanocomposites.

Another excellent property of the $TiO_2$—RGO is high rate capacity. The results are shown in Fig. 6, in which rates of up to 10 C have been applied. The cell was first cycled at 0.2 C and after 5 cycles, the rate was increased in stages to 10 C. A specific capacity of about 346.8 mA h/g was obtained at a rate of 0.2 C after 5 cycles; this value decreases to 237.4 mA h/g at 1 C after 5 cycles, 203.1 mA h/g at 2 C after 5 cycles, 148.5 mA h/g at 10 C after 5 cycles, and finally, back to 330.6 mA h/g at 0.2 C after 5 cycles [35]. The high rate capability can be attributed to the transport advantages of the unique structure of RGO, such as short transport paths for the $Li^+$ ions and electrons, as well as a high electrode—electrolyte contact area, i.e., more electroactive sites.

In order to test the cyclability at high rate and elucidate the effect of RGO on the $TiO_2$—RGO nanocomposites, LIBs made using $TiO_2$—RGO and $TiO_2$ were run at 10 C for 100 cycles under the same conditions, respectively (Fig. 7). As can be seen, both the $TiO_2$—RGO and $TiO_2$ show superior cycling performance over extended cycling. It shows that $TiO_2$—RGO starts at 295.4 mA h $g^{-1}$ and still remains at 112.3 mA h $g^{-1}$ after 100 cycles, with a capacity loss of 61.9%, while the capacity of $TiO_2$

starts at 75.6 mA h $g^{-1}$ and only remains at 12.6 mA h $g^{-1}$ after 100 cycles, with a capacity loss of 83.3%. The initial reversible capacity (2nd cycle) of $TiO_2$ only amounts to 34.2% of that of $TiO_2$—RGO, while the reversible capacity after 100 cycles of $TiO_2$ only amounts to 11.2% of that of $TiO_2$—RGO, suggesting that the RGO indeed functions with enhanced effect for $TiO_2$—RGO compared with $TiO_2$, not only for the capacity but also for the cyclability.
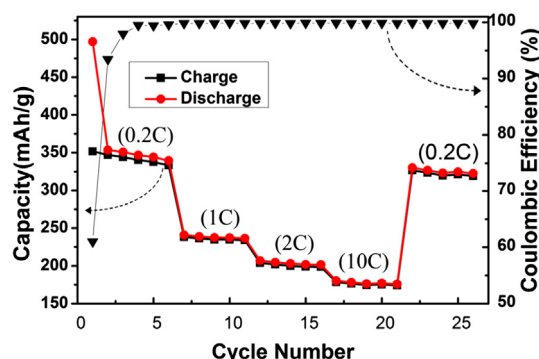


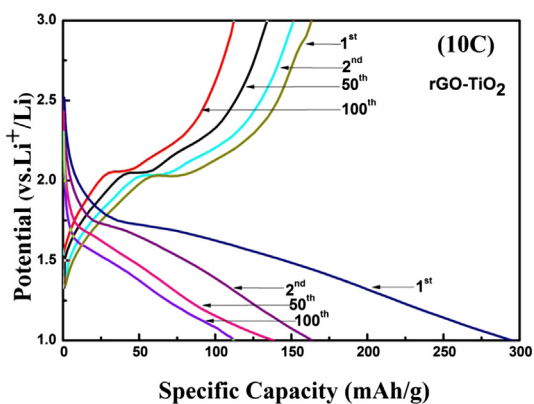Fig. 6 — The charge—discharge performances of $TiO_2$—RGO at various current rates (0.2—10 C).



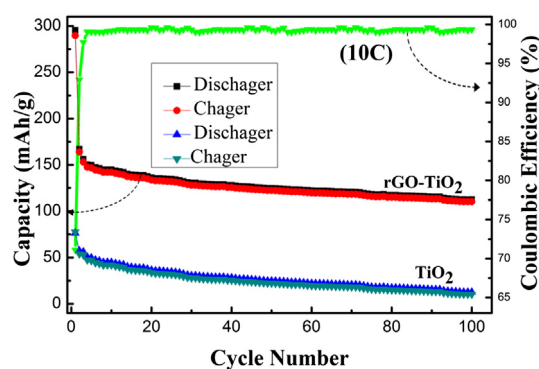Fig. 5 — The charge—discharge curves of the electrode fabricated with $TiO_2$—RGO at a current rate of 10 C.



Fig. 7 — The cycle performance of $TiO_2$—RGO and $TiO_2$ at a current rate of 10 C.

In order to get insight into the remarkable rate performance of the $TiO_2-$ RGO nanocomposites with pure $TiO_2$ without reduced graphene oxide, we carried out electrochemical impedance spectra (ESI) studies on the cell comprising the samples as the working electrode vs. Li without discharge and charge cycles before cycles (bc-$TiO_2$, bc-$TiO_2$-RGO respectively) and after 10 discharge and charge cycles (ac-$TiO_2$, ac-$TiO_2$-RGO respectively) in Fig. 8. The results are given as Nyquist plots (Z′ vs. −Z″), where Z′ and Z″ refer to the real and imaginary parts of the cell impedance, respectively. We can observe one semicircle in the high frequency range and a sloping straight line in the low frequency range in the two Nyquist plots. An intercept at the Z′ axis at high frequency is related to the resistance of the electrolytes. The radius of the semicircles of the $TiO_2-$RGO electrode is smaller than that of the pure $TiO_2$ electrode, suggesting that the charge-transfer resistance of $TiO_2-$RGO is lower than that of the pure $TiO_2$ electrode [36]. The values of the Ohmic resistance and charge-transfer resistance before cycling are 13.2 and 186.4 Ohm for $TiO_2-$RGO, respectively, which are remarkably lower than those of the corresponding $TiO_2$ 15.3 and 242.3 Ohm, respectively. The values of the Ohmic resistance and charge-transfer resistance after 10 cycles are 5.52 and 41.5 Ohm for $TiO_2-$RGO, respectively, which are lower than those of the corresponding $TiO_2$ (13.2 and 105.2 Ohm, respectively).

## 4. Conclusions

Insufficient conductivity and theoretical capacity of $TiO_2$ are the main drawbacks for its practical application in Li-ion batteries. In this work, the mixed crystal phases of nano-rod $TiO_2$/GNS composites with small particle size were hydrothermally synthesized. Compared with that of corresponding pure $TiO_2$ samples, the conductivity of $TiO_2-$RGO nanocomposites was enhanced by anchoring the mixed crystal phases of $TiO_2$ on the RGO sheets and removing the oxygen-containing functional groups. As the anode material of lithium ion batteries, $TiO_2-$RGO nanocomposites exhibit high rate capacity because the RGO could also contribute specific capacity without the problem of graphene sheet restacking.
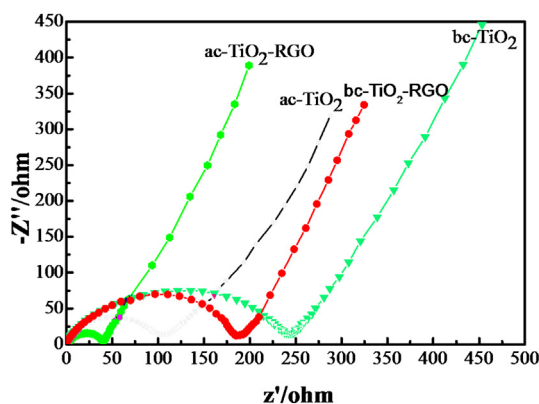
**Fig. 8** − Electrochemical impedance spectra of $TiO_2-$RGO and pure $TiO_2$ electrodes before cycles (bc-$TiO_2$, bc-$TiO_2-$RGO), after ten cycles (ac-$TiO_2$, ac-$TiO_2-$RGO).

The synthesis process is simple and versatile, and could be extended to other metal oxide−graphene anode materials used in lithium ion batteries.

REFERENCES

[1] Chen JS, Archer LA, Lou XW. $SnO_2$ hollow structures and $TiO_2$ nanosheets for lithium-ion batteries. J Mater Chem 2011;21:9912−24.

[2] Tollefson J. Car industry: charging up the future. Nature 2008;456:436−40.

[3] Xu MQ, Hao LS, Liu YL, Li WS, Xing LD, Li B. Experimental and theoretical investigations of dimethylacetamide (DMAc) as electrolyte stabilizing additive for lithium ion batteries. J Phys Chem C 2011;115:6085−94.

[4] Qiu Y, Yan K, Yang S, Jin L, Deng H, Li W. Synthesis of size-tunable anatase $TiO_2$ nanospindles and their assembly into anatase@titanium oxynitride/titanium nitride-graphene nanocomposites for rechargeable lithium ion batteries with high cycling performance. ACS Nano 2010;4:6515−26.

[5] Md. Selim Arif Sher Shah ARP, Zhang Kan, Hyeok Park Jong, Yoo Pil J. Green synthesis of biphasic $TiO_2$-reduced graphene oxide nanocomposites with highly enhanced photocatalytic activity. ACS Appl Mater Interfaces 2012;2012:3893−901.

[6] Yi J, Lu DS, Li XP, Hu SJ, Li WS, Lei JF, et al. Preparation and performance of porous titania with a trimodal pore system as anode of lithium ion battery. J Solid State Electrochem 2012;16:443−8.

[7] Kang JW, Kim DH, Mathew V, Lim JS, Gim JH, Kimz J. Particle size effect of anatase $TiO_2$ nanocrystals for lithium-ion batteries. J Electrochem Soc 2011;158:A59−62.

[8] Wagemaker M, Borghols WJH, Mulder FM. Large impact of particle size on insertion reactions. A case for anatase $Li_xTiO_2$. J Am Chem Soc 2007;129:4323−7.

[9] Wagemaker M, Kearley GJ, van Well AA, Mutka H, Mulder FM. Multiple li positions inside oxygen octahedra in lithiated $TiO_2$ anatase. J Am Chem Soc 2003;125:840−8.

[10] Li JR, Tang ZL, Zhang ZT. Preparation and novel lithium intercalation properties of titanium oxide nanotubes. Electrochem Solid State Lett 2005;8:A316−9.

[11] Wang HL, Cui LF, Yang YA, Casalongue HS, Robinson JT, Liang YY, et al. $Mn_3O_4$-graphene hybrid as a high-capacity anode material for lithium ion batteries. J Am Chem Soc 2010;132:13978−80.

[12] Wang DH, Choi DW, Li J, Yang ZG, Nie ZM, Kou R, et al. Self-assembled $TiO_2$-graphene hybrid nanostructures for enhanced li-ion insertion. ACS Nano 2009;3:907−14.

[13] Qiu JX, Zhang P, Ling M, Li S, Liu PR, Zhao HJ, et al. Photocatalytic synthesis of $TiO_2$ and reduced graphene oxide nanocomposite for lithium ion battery. ACS Appl Mater Interfaces 2012;4:3636−42.

[14] He LF, Ma RG, Du N, Ren JG, Wong TL, Li YY, et al. Growth of $TiO_2$ nanorod arrays on reduced graphene oxide with enhanced lithium-ion storage. J Mater Chem 2012;22:19061–6.

[15] Cao HQ, Li BJ, Zhang JX, Lian F, Kong XH, Qu MZ. Synthesis and superior anode performance of $TiO_2$@reduced graphene oxide nanocomposites for lithium ion batteries. J Mater Chem 2012;22:9759–66.

[16] Marcano DC, Kosynkin DV, Berlin JM, Sinitskii A, Sun ZZ, Slesarev A, et al. Improved synthesis of graphene oxide. ACS Nano 2010;4:4806–14.

[17] Li BJ, Cao HQ. ZnO@graphene composite with enhanced performance for the removal of dye from water. J Mater Chem 2011;21:3346–9.

[18] Zhang H, Lv XJ, Li YM, Wang Y, Li JH. P25-graphene composite as a high performance photocatalyst. ACS Nano 2010;4:380–6.

[19] Li BJ, Cao HQ, Shao J, Qu MZ. Enhanced anode performances of the $Fe_3O_4$-carbon-rGO three dimensional composite in lithium ion batteries. Chem Commun 2011;47:10374–6.

[20] Kment S, Gregora I, Kmentova H, Novotna P, Hubicka Z, Krysa J, et al. Raman spectroscopy of dip-coated and spin-coated sol-gel $TiO_2$ thin films on different types of glass substrate. J Sol-Gel Sci Technol 2012;63:294–306.

[21] Kim CH, Kim BH, Yang KS. $TiO_2$ nanoparticles loaded on graphene/carbon composite nanofibers by electrospinning for increased photocatalysis. Carbon 2012;50:2472–81.

[22] Wang J, Zhou Y, Xiong B, Zhao Y, Huang X, Shao Z. Fast lithium-ion insertion of $TiO_2$ nanotube and graphene composites. Electrochim Acta 2013;88:847–57.

[23] Zhang XY, Sun YJ, Cui XL, Jiang ZY. A green and facile synthesis of $TiO_2$/graphene nanocomposites and their photocatalytic activity for hydrogen evolution. Int J Hydrogen Energy 2012;37:811–5.

[24] Chen XB, Lou YB, Samia ACS, Burda C, Gole JL. Formation of oxynitride as the photocatalytic enhancing site in nitrogen-doped titania nanocatalysts: comparison to a commercial nanopowder. Adv Funct Mater 2005;15:41–9.

[25] Liu CM, Sun H, Yang SH. From nanorods to atomically thin wires of anatase $TiO_2$: nonhydrolytic synthesis and characterization. Chem Eur J 2010;16:4381–93.

[26] Matranga C, Chen L, Smith M, Bittner E, Johnson JK, Bockrath B. Trapped $CO_2$ in carbon nanotube bundles. J Phys Chem B 2003;107:12930–41.

[27] Jensen H, Soloviev A, Li ZS, Sogaard EG. XPS and FTIR investigation of the surface properties of different prepared titania nano-powders. Appl Surf Sci 2005;246:239–49.

[28] Zhang F, Cao HQ, Yue DM, Zhang JX, Qu MZ. Enhanced anode performances of polyaniline-$TiO_2$-reduced graphene oxide nanocomposites for lithium ion batteries. Inorg Chem 2012;51:9544–51.

[29] Yu Y, Gu L, Wang CL, Dhanabalan A, van Aken PA, Maier J. Encapsulation of Sn@carbon nanoparticles in bamboo-like hollow carbon nanofibers as an anode material in lithium-based batteries. Angew Chem Int Ed 2009;48:6485–9.

[30] Subramanian V, Karki A, Gnanasekar KI, Eddy FP, Rambabu B. Nanocrystalline $TiO_2$ (anatase) for Li-ion batteries. J Power Sources 2006;159:186–92.

[31] Wang J, Zhou Y, Hu Y, O'Hayre R, Shao Z. Facile synthesis of nanocrystalline $TiO_2$ mesoporous microspheres for lithium-ion batteries. J Phys Chem C 2011;115:2529–36.

[32] Liang C, Dudney NJ, Howe JY. Hierarchically structured sulfur/carbon nanocomposite material for high-energy lithium battery. Chem Mater 2009;21:4724–30.

[33] Hu YS, Kienle L, Guo YG, Maier J. High lithium electroactivity of nanometer-sized rutile $TiO_2$. Adv Mater 2006;18:1421.

[34] Park WI, Lee C-H, Lee JM, Kim N-J, Yi G-C. Inorganic nanostructures grown on graphene layers. Nanoscale 2011;3:3522–33.

[35] Sudant G, Baudrin E, Larcher D, Tarascon JM. Electrochemical lithium reactivity with nanotextured anatase-type $TiO_2$. J Mater Chem 2005;15:1263–9.

[36] Yang S, Feng X, Muellen K. Sandwich-like, graphene-based titania nanosheets with high surface area for fast lithium storage. Adv Mater 2011;23:3575.